

1 **A grid implementation of the SLUTH algorithm for visualizing the depth and structural index of**  
2 **magnetic sources**

3 Richard S. Smith, Department of Earth Sciences, Laurentian University, 935 Ramsey Lake Road,  
4 Sudbury, Ontario, Canada, P3E 2C6. [RSSmith@laurentian.ca](mailto:RSSmith@laurentian.ca) phone +1 705 675 1151 (corresponding  
5 author)

6 Jeffrey B. Thurston, 3628 7A St SW, Calgary, Alberta, Canada, T2T 2Y5 [jbthurston@gmail.com](mailto:jbthurston@gmail.com)

7 Ahmed Salem, GETECH, Kitson House, Elmete Hall, Elmete Lane, Leeds, LS8 2LJ, UK and Nuclear  
8 Materials Authority, PO Box 530 Maadi, Cairo, Egypt. [Ahmed.Salem@getech.com](mailto:Ahmed.Salem@getech.com)

9 Alan B. Reid, School of Earth & Environment, University of Leeds, and Reid Geophysics Ltd., 7 Keymer  
10 House, Michel Grove, Eastbourne, BN21 1JZ, United Kingdom. [alan@reid-geophys.co.uk](mailto:alan@reid-geophys.co.uk)

11

12 This document is the accepted manuscript. The version of record is cited and available as follows

13 Smith, R.S., Thurston, J.B., Salem, A. and Reid, A.B., 2012, A grid implementation of the SLUTH  
14 algorithm for visualizing the depth and structural index of magnetic sources: Computers and Geosciences,  
15 44, 100-108. <http://dx.doi.org/10.1016/j.cageo.2012.03.004>

16

17

18 **Abstract**

19 The SLUTH method requires first-order derivatives at two or more different heights above the ground and  
20 can estimate the location and depth of source bodies from magnetic data. Results of this method are  
21 independent of a specific model type and can be used to estimate the most appropriate model (structural  
22 index). This paper presents a grid implementation of the SLUTH method to visualize both depth and  
23 structural index from magnetic anomaly data. The implementation uses the Geosoft GX programming  
24 language. The method has been tested using theoretical magnetic gridded data and of two methods have  
25 been used for estimating depth; the estimate from the width of the imaged feature gives an underestimate  
26 and the estimate from the rate of fall off of the field with height gives an overestimate. The practical  
27 utility of the algorithm is demonstrated using field data from the Saskatoon area of Canada.

28 **Keywords:** automatic; interpretation; image; basement; structure

29 **Introduction**

30 In recent years a number of methods have been introduced for extracting source parameters from  
31 magnetic data. The commonly used methods are Euler deconvolution (Ruddock et al., 1966; Thompson,  
32 1982; Reid et al., 1990), the Naudy method (Naudy, 1971), Werner deconvolution (Hartman et al., 1971),  
33 the analytic signal method (Nabighian, 1972; Roest et al., 1992) and use of the local wavenumber  
34 (Thurston and Smith, 1997; Keating, 2009). In recent years the use of “similarity transforms” has also  
35 been proposed for interpreting magnetic data (Stavrev et al., 2009; Gerovska et al., 2010). Most of the  
36 methods use spatial derivatives of the magnetic field and generally require some assumption about the  
37 shape of the causative body. Methods that relax assumptions about the shape of the causative body often  
38 require higher-order derivatives (Smith et al., 1998; Thurston et al., 2002; Salem et al., 2005; Salem et al.,  
39 2008) which can be problematic as the calculation of the higher-order derivative can amplify noise in the  
40 data.

41 A patent application in 1966 (Ruddock et al., 1966) suggested using the magnetic field measured at two  
42 different heights to allow the calculation of a vertical derivative. In recent years a number of magnetic  
43 interpretation techniques have been introduced that also use data at multiple heights. Application of these  
44 methods, to surveys acquired at a single sensor elevation, requires numerical continuation to a greater  
45 height (Dean, 1958). Like introducing higher-order derivatives into the methods, introducing  
46 continuation also provides a means for constraining the source geometry. However, unlike gradient  
47 computation, upward continuation does not introduce instability due to amplification of high-frequency  
48 noise (Lahti and Karinen, 2010). Techniques which use wavelets (Moreau et al., 1997; Hornby et al.,  
49 1999; Sailhac et al., 2000; Vallee et al., 2004; Fedi, 2007; Cella et al., 2009; Sailhac et al., 2009) use  
50 upward continuation implicitly or explicitly and are also able to estimate the causative structure.

51 The calculation of higher-order derivatives requires special attention (Pasteka et al., 2009); this is  
52 particularly so for gridded data, which is generally derived from profile data by sub-sampling and  
53 interpolation. Thus, a group of workers have proposed calculating the derivatives from profile data  
54 (Salem and Smith, 2005; Smith and Salem, 2005; Smith et al., 2005) as the lateral spacing of the samples  
55 is finer and the signal fidelity is higher on profile data than it is on gridded data. However, displaying  
56 these profile results on an image is not straightforward.

57 The SLUTH method proposed by Thurston and Smith (2007) and implemented by Ulla et al. (2010) uses  
58 upward-continued data and only requires first-order derivatives, so it is more robust in the presence of  
59 noise than the methods that require higher-order derivatives. The Ulla et al. implementation is tailored  
60 specifically to profile data, but the SLUTH method could also be implemented on grids as first-order  
61 derivatives can normally be calculated fairly well on gridded data. The advantage of grid implementation  
62 is the ability to display the results in a manner that can be easily visualized and incorporated with other  
63 geological and geophysical maps. To this end, we have chosen to display the results using the same  
64 display approach as the tilt-depth method of Salem et al. (2007, 2010). The resulting images can be

65 obtained without reduction to the pole or the calculation of higher-order derivatives, nor are they also  
66 only valid for vertical contacts; all of which are restrictions of the tilt-depth method.

67 We have chosen to implement SLUTH in the Geosoft GX language (or API), allowing all users of the  
68 Geosoft montaj geophysical software to run the method. The input to the algorithm is gridded magnetic  
69 data on two height levels (the acquisition height and an upward continued height) plus the associated  
70 vertical and horizontal derivatives. Geosoft montaj has a GX tool (mapmap1) for upward continuing the  
71 data and calculating all the required spatial derivatives. The GX is available from [www.iamg.org](http://www.iamg.org). The  
72 source code is also available for those who would like to translate the code and implement the algorithm  
73 in another environment.

#### 74 **The Method**

75 The SLUTH method (Thurston and Smith, 2007, Ulla et al., 2010) uses the quantity  $m$  which is the  
76 negative of the ratio of the horizontal to the vertical derivatives

$$77 \quad m = -\frac{dT/dx}{dT/dz}, \quad (1)$$

78 where  $T$  is the total magnetic field,  $z$  is the vertical direction, and  $x$  is the horizontal direction. The  
79 quantity  $m$  is the inverse of the ratio used in the tilt angle quantity proposed by Miller and Singh (1994)  
80 and utilized by Salem et al. (2007) in their tilt-depth method. Hence small values of the tilt angle  
81 correspond to large values of  $m$ . The procedure requires that the magnetic field and its horizontal and  
82 vertical derivatives be known on one or more datums (or heights) at or above the earth's surface. Figure 1  
83 shows an aeromagnetic-survey aircraft and the datum along which the measurements are acquired. The  
84 derivatives could be measured or calculated. Also shown in Figure 1 is a second (higher) level, in this  
85 case called the upward continued datum, as the measurements at this level can be calculated by upward  
86 continuation (Dean, 1958) from the values on the lower measurement datum. However, the field values  
87 and the derivatives could also be measured on this datum. The quantity  $m$  is calculated at all locations on

88 the measurement and upward continued datums, and then similar values of  $m$  are sought on the upper and  
89 lower datums. Figure 1 shows the locations of three pairs of identical values on the lower and upper  
90 datums. The first pair consists of a value  $m_{al}$  on the lower datum that is equal to the value  $m_{au}$  on the  
91 upper datum. Joining these two locations creates a ray. Similarly, rays can be drawn through the pairs  
92  $(m_{bl}, m_{bu})$  and  $(m_{cl}, m_{cu})$ . For homogeneous sources, these rays intersect at the location of the magnetic  
93 source body (Thurston and Smith, 2007). Note that this procedure can be applied for more than three  
94 pairs and more than two datums. The angle that the ray makes with a vertical line is important. Figure 1  
95 shows the angle from the vertical  $\theta_c$  for the ray associated with the pair  $(m_{cl}, m_{cu})$ . If the angle  $\theta_c$  is  
96 zero, then the ray is directly above the source of the magnetic anomaly. Thurston and Smith (2007) and  
97 Ulla et al. (2010) assumed that the sources were two dimensional and perpendicular to the flight lines.  
98 This means that the rays drawn on Figure 1 are actually planes that extend in and out of the page.

#### 99 *Grid implementation*

100 Figure 2 shows an oblique 3D view of part of the measurement datum and part of the upward continued  
101 datum. Eighteen grid points are shown on each datum, but the grid will extend outward in all four  
102 directions. The dark point on the measurement datum shows a specific point and the dashed line joins  
103 this point to the corresponding point directly above on the upward continued datum. Surrounding this  
104 central point are eight nearby points, four in the cardinal directions and four on diagonal or inter-cardinal  
105 directions. In the upper datum surface, solid lines have been drawn in the cardinal directions joining  
106 these nine points.

107 The value of  $m$  is calculated at the central point on the lower datum, and then the locations where similar  
108  $m$  value occurs on the upper datum are estimated. This can be done using a variety of approaches, but we  
109 have chosen to use linear interpolation between the points along the solid lines. Figure 3 shows four dots  
110 on the upper datum that have similar  $m$  values to the central value on the lower datum. These four points  
111 define a line which we call the strike line. The strike line and the lower central point together form a *ray*

112 *plane*, shown on Figure 3 as a shaded plane. In some cases there may only be one, two or three location  
 113 on the upper datum where the  $m$  values are the same as the central  $m$  value on the lower datum. In cases  
 114 when there are more than two points, the degree of misfit from a straight line could be used as a measure  
 115 of the noise in the data or of the quality of fit and hence the validity of the assumption that the model is a  
 116 2D homogeneous source. If the model is 2D, the direction of the horizontal gradient vector should be  
 117 perpendicular to the strike direction. The deviation of this angle from 90 degrees could also be used as a  
 118 measure of when the model is not two dimensional.

119 The strike line is horizontal and thus it defines the strike direction of the 2D structure. The cross product  
 120 of this strike direction and any other non-horizontal vector in the ray plane gives the normal to the plane.  
 121 One choice for the non-horizontal vector is a vector  $A$  that goes from the central point on the lower datum  
 122 to a point on the strike line on the upward continued datum. Figure 4 shows these two vectors and the  
 123 cross product that is normal to the plane. A vector in the dip direction is the cross product of the strike  
 124 vector with the normal vector (Figure 5). To ensure that the dip vector is pointing down, the  $z$  component  
 125 should be pointing down. If not, multiply the dip vector by negative one. The angle of the ray plane from  
 126 the vertical can be obtained by calculating the dot product of the dip vector with the vertical vector.

### 127 *Depth to source*

128 It is possible to estimate the distance  $r$  from the source to the central point on the lower measurement  
 129 datum. This is obtained using the relations for homogeneous functions.

$$130 \quad T(cr) = c^n T(r), \quad (2)$$

$$131 \quad \frac{dT}{dz}(cr) = c^{n-1} \frac{dT}{dz}(r), \quad (3)$$

132 or,

$$133 \quad \frac{dT}{dx}(cr) = c^{n-1} \frac{dT}{dx}(r), \quad (4)$$

134 where  $r$  is a distance from the point that defines the magnetic source and  $c$  is a scale factor. The value of  
 135  $T$  (or the derivatives) at  $r$  are the known values at the central point on the lower datum. The values of  $T$   
 136 (and the derivatives) on the strike line on the upper datum can be calculated by interpolation from the  
 137 known values at the grid nodes. These values are at a distance  $cr$  from the source. From these values, the  
 138 scale factor  $c$  can be estimated from

139 
$$c = \frac{T(cr)/T(r)}{\frac{dT}{dx}(cr)/\frac{dT}{dx}(r)}, \quad (5)$$

140 and/or

141 
$$c = \frac{T(cr)/T(r)}{\frac{dT}{dz}(cr)/\frac{dT}{dz}(r)}. \quad (6)$$

142 In equations (4), (5) and (6), the  $x$  derivative is actually the total horizontal derivative  $\sqrt{\left(\frac{dT}{dx}\right)^2 + \left(\frac{dT}{dy}\right)^2}$ .

143 The distance from the point on the lower datum up the dip vector to the point where it intersects with the  
 144 upper datum (Figure 6) is  $\Delta r$ . From the definition of  $\Delta r$  and  $c$ , we have  $cr=r+\Delta r$ , so

145 
$$r = \frac{\Delta r}{c-1}. \quad (7)$$

146 The depth  $d$  to the source from the lower measurement datum is (Figure 7)

147 
$$d = r \cos \theta, \quad (8)$$

148 where  $\theta$  is the angle from the vertical to the ray plane (Figure 6 and 7).

149 *Structural Index*

150 Using equation (3) or (4), it is possible to calculate the structural index or degree of inhomogeneity  $n$ .

151 The value of  $n$  at each grid point can be calculated from equations (2), (3) or (4). For example

152 
$$n = \ln\left(\frac{T(cr)}{T(r)}\right)/\ln(c), \quad (9)$$

153 or

154 
$$n = \frac{\ln\left(\frac{dT(zr)/dz}{dT(r)/dz}\right)}{\ln(c)} + 1 . \quad (10)$$

155 *Algorithm*

156 The SLUTH grid implementation requires that the field and the spatial derivatives be known on the upper  
157 and lower measurement datums. These can be calculated by upward continuation of the field from the  
158 lower datum to the upper datum. On each datum the spatial derivatives are calculated from the total field.  
159 We found that calculating the vertical derivative in the frequency domain and horizontal derivatives in the  
160 space domain can lead to inconsistent results because the characteristic points on the curve were shifted  
161 relative to where they should be. We found that good results were obtained when all the derivatives and  
162 the upward continuation are calculated in the frequency domain. This can be done in the Geosoft Oasis  
163 montaj software package using the “magmap1” GX. Whenever frequency-domain operations are  
164 performed on grids that will be added/subtracted or otherwise operated on, the best results will be  
165 obtained when the same padding, extrapolation and low pass filtering are applied to all the grids.

166 The following procedure is then applied at each grid point:

- 167 1) Calculate the  $m$  values on the lower and upper datums
- 168 2) Find the  $m$  value at the central point on the lower measurement datum.
- 169 3) Look for locations of similar values on the upper datum and fit a straight line to these upper datum  
170 locations to determine the strike direction of the ray plane. The misfit from the line-fitting will provide an  
171 estimate of the error. When there are three or more locations, there will be three or more strikes that we  
172 can calculate and our simple way of estimating the error is to calculate the standard deviation of these  
173 strikes. More sophisticated ways are possible.
- 174 4) Calculate the normal to the ray plane, the dip vector and the angle of the dip vector from the vertical,  $\theta$ .

175 5) Estimate  $c$  using the values of  $T$  and the derivatives at the lower central point and the values on the  
176 upper datum.

177 6) Estimate  $\Delta r$  and then the distance  $r$  of the lower grid point to the source and then the corresponding  
178 depth  $d$ .

179 7) Estimate the structural index.

180 This procedure has been implemented as a Geosoft GX called gridsluth that can be run within the Oasis  
181 Montaj geophysical data processing software. The output from the GX are grids of the strike in degrees  
182 from north, the standard deviation of the strike, the structural index, and the depth. The latter are output  
183 in grid cell units, so must be converted to dimensioned units by multiplying by the grid cell spacing in the  
184 appropriate dimensioned units.

#### 185 *Display of results*

186 The derived quantities (for example, depth, fit, structural index, strike, angle of ray plane from vertical)  
187 can be estimated at all grid points. However, it only makes sense to display the results when the grid cell  
188 is judged to be close to a magnetic source. The grid cells are close to the magnetic source when the ray  
189 plane is close to vertical. Our approach is to display the results using a method similar to that proposed  
190 by Salem et al. (2007), who made the map dark where the tilt angle was less than 45 degrees, creating a  
191 zone on the map twice as wide as the depth to the source. In our implementation, the data on the lower  
192 measurement datum will be upward continued 1 or 2 grid cell spacings. Figure 8 shows the case when it  
193 is two grid cell spacings, when a dip angle of 27 degrees or less ensures that the ray plane intersects the  
194 upper datum between the central point and the nearest grid point (s). The grid locations where the ray  
195 plane is less than 27 degrees will be coloured. This will create a zone with a width equal to the depth to  
196 the source below the measurement datum. The colour of the zone could be set according to the numerical  
197 value of any of the derived quantities (for example, structural index or standard deviation of the strike). It  
198 is also possible to colour the image according to the depth and strike and dip angles; however, this

199 information will be somewhat redundant as the same information will already be evident from the shape  
200 of the coloured areas. One advantage of displaying this redundant information is that the consistency of  
201 the parameters will give an indication of how good the model is and how well the method is working in  
202 this area.

203 Poor solutions will also be obtained when our assumptions are not satisfied. We have assumed that the  
204 magnetic sources are 2D and the structural indices of 2D magnetic sources range between 0 and 2.  
205 However structural index values of 3 are also valid for dipole (3D) sources (Stavrev and Reid, 2007). If  
206 the 3D sources are sufficiently deep and the spatial derivatives are adequately sampled on the grid, then  
207 there may be some information in the processed data that could be extracted so as to assist in an  
208 interpretation. So, rather than only displaying solutions with valid 2D indices between 0 and 2, we have  
209 elected to display the results for indices less than zero and greater than 3. In order to allow some margin  
210 for errors, we restrict the valid range of structural indices from -0.5 to 3.5.

211

## 212 **Synthetic examples**

213 A synthetic data set presented by Salem et al. (2008) has been used to test the grid implementation of the  
214 SLUTH method.

215 Figure 9 shows the magnetic field on the lower datum. The long linear feature is a vertical thin dike at a  
216 depth of 5 km with a magnetization of 5 A/m; the smaller body (top right) is a vertical sided prism at a  
217 depth of 3 km and a magnetization of 0.4 A/m; and the larger body (bottom right) is a vertical prism with  
218 a magnetization of 0.6 A/m and a depth to top of 7 km. The magnetization is induced by a field inclined  
219 at 90 degrees. The  $m$  values on the lower datum are shown on Figure 10, the image of the  $m$  values on the  
220 upper datum look very similar, but the values differ slightly. Applying the SLUTH algorithm, gives the  
221 results displayed on Figures 11 to 14. The strike angle is shown on Figure 11, where zero degrees  
222 corresponds to a north-south strike, 90° is east west and 180° is also north south. The colours correspond

223 to the correct strike of the features on the map. The standard deviation of the strike is shown on Figure  
224 12. Generally the deviations are less than  $0.6^\circ$ , except at the source-body vertices, where a poor estimate  
225 of the strike is expected as the model departs significantly from being two dimensional. The structural  
226 index is shown on Figure 13. The vertical prisms are approximately 2D contacts close to the centre of  
227 each edge, so the structural index should be close to zero and this is almost the case (the index is  
228 about 0.35), but towards the vertices, the index increases to about 0.7. The estimated index for the dike is  
229 about 1.1, which is close to the expected value of 1.0. The depth is shown on Figure 14. The dike model  
230 has colours that indicate a depth of 5.5 km (c.f. 5 km), the top prism has colours corresponding to depths  
231 about 4 km (c.f. 3 km) in the centres of the edges and larger towards the vertices. The bottom prism has  
232 depths of 10 km or more (c.f. 7 km). In all cases the depths derived from equation 8 are overestimates;  
233 however, the depths from the width of the zone that is coloured are not overestimates. In fact, the zone  
234 associated with the top prism is actually 2.5 km wide, the width of the dike is 4.5 km and the width of the  
235 bottom prism is 6 km. There are difficulties in reading widths from the images, as Geosoft interpolates  
236 between grid values on images and it is not clear how it deals with displaying null values and grid cells  
237 next to null values. Given the above results, we should emphasize that the SLUTH grid images should be  
238 used to identify relative changes in the source parameters and not for determining the exact value. If the  
239 exact values are required, then the data should be modelled.

240 On Figures 11 to 14 there are coloured artifacts on the edges of the images that are not associated with the  
241 three bodies. These are where the magnetic field is small and hence the gradients will be small. We  
242 should therefore expect noise artifacts such as these in areas where the magnetic field are weak or  
243 relatively flat.

244

## 245 **Field examples**

246 *Saskatoon Area*

247 The grid implementation of the SLUTH method has been tested on field data collected by the GSC in the  
248 Saskatoon area of Canada (Geological Survey of Canada, 1995). Figure 15 shows the total magnetic field  
249 data over an area 143 km wide by 117 km high. The aircraft flight height was 150 m, the flight lines are  
250 east-west at a spacing of 800 m and the grid cell size is 200 m. A scale bar is shown at the bottom left  
251 and the colour bar is at the top right. The basement in this part of the Western Canada Sedimentary Basin  
252 is largely unexplored; however, broadly speaking, the primary non-magnetic Phanerozoic sediments in  
253 this part of southern Saskatchewan extend from surface to about 1200 m below surface in the top right to  
254 1800 m below surface at bottom left (Saskatchewan Geological Survey, 1999). There are strong magnetic  
255 features evident in the image, a magnetic high on the eastern side of the image, a magnetic low and a  
256 wedge of high magnetic material in the centre. This wedge is widest at the north and narrows to the  
257 south. Also marked with asterisk symbols are three narrow features. These magnetic features are  
258 associated with basement rocks, probably the Proterozoic Reindeer zone, which outcrops to the north.  
259 Figure 16 is an image of the structural index of the magnetic sources. The map is largely blue (less than  
260 0.35), indicating that most features are contacts or faults separating one relatively wide domain from  
261 another wide domain. There are a number of structures with indices greater than 1.0. Note that these  
262 correspond to the narrower features marked with asterisks, so they could be dykes or ribbon models. The  
263 depth image (Figure 17) shows that the principal features are 1.5 km deep or deeper, which is consistent  
264 with the depth to basement in the area. These depths are consistent with the width of the features which  
265 seem to be about 3 km wide. The zones of weak magnetic response (blue zones on Figure 15) correspond  
266 with pink zones in figure 17, implying that the magnetic sources are much deeper in these areas.  
267 However, these blue zones on Figure 15 are where the magnetic field is weak, so we should not  
268 necessarily pay too much attention to these results, as the synthetic modelling implies we might see noise  
269 artifacts in these zones. This zone could represent a basement low not identified on the geological map  
270 (Saskatchewan Geological Survey, 1999). The basement depths are interpreted to increase to the south,  
271 but this is not clearly evident in the depth image (Figure 17). One possible explanation for this is that the  
272 strongest magnetic features are coming from sources below the sediment/basement interface. Note that

273 there are many strong features adjacent to each other in the magnetic data, so interference will be a  
274 problem when interpreting this data set.

275 The depth results on Figure 17 show some artefacts aligning with the east-west flight lines. More careful  
276 gridding of the data could reduce these artefacts. Also, filtering of the resultant image could remove  
277 some of the single point features and ragged nature of the image. However, we have elected not to do  
278 this, so that the reader can see the raw unadulterated results.

279 An example of the type of information that can be extracted from these images can be inferred by looking  
280 at the asterisk on the upper left of the image. Above the asterisk, there is a stronger magnetic feature and  
281 below the asterisk the feature is weaker. The depth information indicates that the depths are similar, so  
282 the stronger magnetic anomaly could be due to more susceptible or thicker material to the north.

283

## 284 **Discussion**

285 The SLUTH method uses only first derivatives, so it is robust to noise compared with methods like the  
286 tilt-angle derivative method (Salem et al., 2008), which require second derivatives and upward  
287 continuation to ensure stability. The disadvantage is that the  $c$  value and hence the depth estimate derived  
288 using equation 7 and 8 use the magnitude of the total field and the first derivatives. If there is interference  
289 from surrounding sources, then the magnetic field and hence the  $c$  value will be distorted and the depth  
290 estimate will also be distorted. The interference can be reduced by using higher-order derivatives (which  
291 are sharper and less subject to interference), but this would involve using first- and second-order  
292 derivatives to estimate the  $c$  value and the depth. The drawback is that these higher-order derivatives are  
293 noisier, making the depth estimate less reliable. Other grid implementations of the SLUTH method using  
294 similar strategies are also possible.

295 A detailed analysis of the robustness of the SLUTH method to interference was undertaken by Ulla et al.  
296 (2010). They showed that there was minimal interference between two vertical dykes when the two

297 dykes were a distance apart that was more than three times the depth that the dyke was buried below the  
298 sensor.

299 Ulla et al. (2010) also analysed the robustness of the SLUTH method to random noise and found that  
300 reasonable estimates of the depth could be obtained when the random noise was less than 1 nT.

301 We have chosen to implement the method using values on two height datums. More complex  
302 implementations could use multiple height datums. One advantage of using multiple datums is that the  
303 additional information can be used to provide an estimate of whether or not the source is homogeneous  
304 (Keating, 2009). This would be possible using our implementation; the program could be run multiple  
305 times, with multiple continuation distances. If the estimated index is similar for all runs, then the source  
306 is homogeneous.

307

## 308 **Conclusions**

309 The SLUTH method has been implemented to run on gridded data as a GX in the Geosoft montaj  
310 geophysical processing package. The inputs to the GX are a grid of the total field on a measurement  
311 datum and the total field on a higher datum, which can be calculated by upward continuation. Also  
312 required are the vertical and horizontal derivatives on both datums. The upward continuation and the  
313 spatial derivatives can be calculated the using the magmap1 GX available in Geosoft Oasis montaj. The  
314 outputs from the algorithm are grids of the strike direction, the standard deviation in the strike direction,  
315 the index and the depth. The grids are white (dummy or null values) where the dip of the ray plane is  
316 greater than 27 degrees. Where the dip is less than 27 the colour is dependent on the strike, strike  
317 standard deviation, index and depth respectively. The depth is also equal to the width of the coloured  
318 zone, so a second estimate of the depth can be obtained by looking at the width of the coloured zone. In  
319 our synthetic example, we found that the colour of the grid gave an overestimate and the width of the  
320 coloured zone a slight underestimate. Of the two estimates, the width appears to be more robust.

321 Nonetheless, variations in colour and widths can be used to map qualitative changes in the depth of  
322 features. The depth information obtained from the Saskatoon magnetic data set did not image the depth to  
323 the basement well for two reasons. 1) Most of the magnetic sources seem to be deeper than the  
324 sediment/basement interface and 2) interference seemed to be a problem. However, it is still possible to  
325 extract source parameter information from the data by looking at the images carefully. In the Saskatoon  
326 area, zones of weak magnetic response are interpreted as due to basement lows.

327

### 328 **Acknowledgements**

329 Richard Smith is grateful to the Industrial Research Chair funded by NSERC, Vale, Xstrata Nickel,  
330 QuadraFNX Mining, Wallbridge Mining Company and the Centre for Excellence in Mining Innovation.

331

### 332 **References**

333 Cella, F., Fedi, M., Florio, G., 2009. Toward a full multiscale approach to interpret potential fields.

334 Geophysical Prospecting 57, 543–557 doi: 10.1111/j.1365-2478.2009.00808.x

335 Dean, W. C., 1958. Frequency analysis for gravity and magnetic interpretation, Geophysics

336 23, 97-127.

337 Fedi, M., 2007. DEXP: A fast method to determine the depth and the structural index of potential fields

338 sources. Geophysics 72, I1–I11, doi:10.1190/1.2399452

339 Geological Survey of Canada, 1995. Aeromagnetic total field map, Saskatchewan: NTS 73B/NW, scale

340 1:100000. GSC open file number 2955. [http://gdr.nrcan.gc.ca/aeromag/index\\_e.php](http://gdr.nrcan.gc.ca/aeromag/index_e.php) (accessed 2

341 September, 2011).

342 Gerovska, D., Araúz-Bravo, M. J., Whaler, K., Stavrev, P., and Reid, A., 2010. Three-dimensional  
343 interpretation of magnetic and gravity anomalies using the finite-difference similarity transform.  
344 *Geophysics* 75, L79–L90. doi: 10.1190/1.3453765

345 Hartman, R. R., Teskey, D.J., and Friedberg, J. L., 1971. A system for rapid digital aeromagnetic  
346 interpretation. *Geophysics* 36, 891-918.

347 Hornby, P., Boschetti, F., and Horowitz, F. G., 1999. Analysis of potential field data in the wavelet  
348 domain. *Geophysical Journal International* 137, 175–196.

349 Keating, P., 2009, Improved use of the local wavenumber in potential-field interpretation. *Geophysics* 74,  
350 L75-L85.

351 Lahti, I. and Karinen, T., 2010. Tilt derivative multiscale edges of magnetic data. *The Leading Edge* 29,  
352 24-29.

353 Miller, H. G. and Singh, V., 1994. Potential field tilt—A new concept for location of potential field  
354 sources. *Journal of Applied Geophysics* 32, 213-217. doi:10.1016/0926-9851(94)90022-1

355 Moreau, F., Gibert, D., Holschneider, M. and Saracco, G., 1997. Wavelet analysis of potential fields.  
356 *Inverse Problems* 13, 165–178.

357 Nabighian, M. N., 1972. The analytic signal of two-dimensional magnetic bodies with polygonal cross-  
358 section: Its properties and use for automated anomaly interpretation. *Geophysics* 37, 507–517.

359 Naudy, H., 1971. Automatic determination of depth on aeromagnetic profiles. *Geophysics* 36, 712–722.

360 Pasteka, R., Richter, F.P., Karcol, R., Brazda, K. and Hajach, M., 2009. Regularized derivatives of  
361 potential fields and their role in semi-automated interpretation methods. *Geophysical Prospecting* 57,  
362 507–516. doi: 10.1111/j.1365-2478.2008.00780.x

363 Reid, A. B., Allsop, J. M., Granser, H., Millet, A. J., and Somerton, I. W., 1990. Magnetic interpretation  
364 in three dimensions using Euler deconvolution. *Geophysics* 55, 80–91.

365 Roest, W. R., Verhoef, J., and Pilkington, M., 1992. Magnetic interpretation using the 3-D analytic signal.  
366 *Geophysics* 57, 116–125.

367 Ruddock, K. A., Slack, H. A. and Breiner, S., 1966. Method for determining depth and fall-off rate of  
368 subterranean magnetic disturbances utilizing a plurality of magnetometers. US patent 3263161.

369 Sailhac, P., Galdeano, A., Gilbert, D., Morcau, F. and Delor, C., 2000. Identification of sources of  
370 potential fields with the continuous wavelet transform: Complex wavelets and application to  
371 aeromagnetic profiles in French Guiana. *Journal of Geophysical Research* 105, 19455-19475.

372 Sailhac, P., Gibert, D. and Boukerbout, H., 2009. The theory of the continuous wavelet transform in the  
373 interpretation of potential fields: a review. *Geophysical Prospecting* 57, 517–525 doi: 10.1111/j.1365-  
374 2478.2009.00794.x

375 Salem A. and Smith, R., 2005. Depth and structural index from normalized local wavenumber of 2D  
376 magnetic anomalies. *Geophysical Prospecting* 53, 83-89.

377 Salem, A., Ravat, D., Smith, R., and Ushijima, K., 2005. Interpretation of magnetic data using an  
378 enhanced local wavenumber (ELW) method. *Geophysics* 70, L7-L12.

379 Salem, A., Williams, S., Fairhead, D., Smith, R. and Ravat, D., 2008. Interpretation of Magnetic data  
380 using tilt-angle derivatives. *Geophysics* 73, L1-L10.

381 Salem, A., Williams, S., Fairhead J.D., Ravat, D., Smith, R., 2007. Tilt-depth method: A simple depth  
382 estimation method using first-order magnetic derivatives. *The Leading Edge* 26, December, 1502-1505.  
383 doi:10.1190/1.2821934

384 Salem, A., Williams, S., Samson, E., Fairhead, D., Ravat, D. and Blakely, R. J., 2010. Sedimentary basins  
385 reconnaissance using the magnetic Tilt-Depth method. *Exploration Geophysics* 41, 198-209.  
386 doi:10.1071/EG10007

387 Saskatchewan Geological Survey, 1999. Geological map of Saskatchewan 1:1000000 Map.  
388 Saskatchewan Industry and Resources, Saskatoon, Saskatchewan.  
389 [http://www.er.gov.sk.ca/adx/asp/adxGetMedia.aspx?DocID=5145,4477,3440,3385,5460,2936,Documents](http://www.er.gov.sk.ca/adx/asp/adxGetMedia.aspx?DocID=5145,4477,3440,3385,5460,2936,Documents&MediaID=13140&Filename=Geological_Map_of_Sask.pdf)  
390 [ts&MediaID=13140&Filename=Geological\\_Map\\_of\\_Sask.pdf](http://www.er.gov.sk.ca/adx/asp/adxGetMedia.aspx?DocID=5145,4477,3440,3385,5460,2936,Documents&MediaID=13140&Filename=Geological_Map_of_Sask.pdf) (accessed 29 August, 2011)

391 Smith, R.S. and Salem, A., 2005. Imaging the depth, structure, and susceptibility from magnetic data: the  
392 advanced source parameter imaging method. *Geophysics* 70, L31-38.

393 Smith, R.S., Salem, A., and Lemieux, J., 2005. An enhanced method for source parameter imaging of  
394 magnetic data collected for mineral exploration. *Geophysical Prospecting* 53, 655–665.

395 Smith, R.S., Thurston, J.B., Dai, T.-F., and MacLeod, I.N., 1998. iSPI™ - the improved source parameter  
396 imaging method. *Geophysical Prospecting* 46, 141-151.

397 Stavrev, P., and Reid, A., 2007, Degrees of homogeneity of potential fields and structural indices of Euler  
398 deconvolution. *Geophysics* 72, L1–L12, doi: 10.1190/1.2400010Stavrev, P., Gerovska, D., Arauzo-  
399 Bravo, M. J., 2009. Depth and shape estimates from simultaneous inversion of magnetic fields and their  
400 gradient components using differential similarity transforms. *Geophysical Prospecting* 57, 707–717 doi:  
401 10.1111/j.1365-2478.2008.00765.x

402 Thompson, D. T., 1982. EULDPH: A new technique for making computer-assisted depth estimates from  
403 magnetic data. *Geophysics* 47, 31–37.

404 Thurston, J., and Smith, R., 2007. Source location using total-field homogeneity: Introducing the SLUTH  
405 method for depth estimation. *The Leading Edge* 26, 1272-1277.

406 Thurston, J.B., and Smith, R.S., 1997. Automatic conversion of magnetic data to depth, dip, and  
407 susceptibility contrast using the SPI(TM) method. *Geophysics* 62, 807-813.

408 Thurston, J.B., Smith, R.S., and Guillon, J.-C., 2002. A multimodel method for depth estimation from  
409 magnetic data. *Geophysics* 67, 555-561.

410 Ulla, J., Smith, R., Samson, C., Vallée, M., 2010. Automation of the SLUTH method: a novel approach to  
411 airborne magnetic data interpretation. *Near Surface Geophysics* 8, 519-528. doi:10.3997/1873-  
412 0604.2010033

413 Vallee, M.A., Keating P., Smith, R.S. and St-Hilaire, C., 2004. Estimating depth and model type using the  
414 continuous wavelet transform of magnetic data. *Geophysics* 69, 191-199.

415

416 **Figure captions**

417 Figure 1. The basic principle of the SLUTH method. The field is measured on a measurement datum and  
418 upward continued to a higher datum. The horizontal and vertical spatial derivatives are calculated on  
419 both datums and the ratio used to calculate the  $m$  values. Rays are drawn along lines joining similar  $m$   
420 values on the two datums and these rays converge at the source location. The angle of the ray from the  
421 vertical is given by the angle  $\theta$ .

422 Figure 2. Oblique 3D view of the upper and lower datums. The dotted line joins a grid point on the  
423 upper datum directly above a point on the lower datum. There are nine points in a window on the upper  
424 datum (including the central point).

425 Figure 3. The  $m$  value at the central point on the lower datum is  $m_{al}$ . Similar values are sought on the  
426 lines joining the 9 points on the upper datum. In this case, there are four points obtained, forming a  
427 straight horizontal line. This line is the strike direction of the ray plane shown in grey, which is the

428 extension to 3D of the rays drawn on Figure 1. The source location is at greater depth on the ray plane,  
429 where this ray plane intersects with another ray plane.

430 Figure 4. The normal to the ray plane can be obtained as the vector normal to any two non-parallel  
431 vectors in the ray plane. In this case, the non-parallel vectors are the strike vector and the vector **A** from a  
432 point on the strike line to the central point on the lower datum.

433 Figure 5. The dip vector is perpendicular to the normal vector and the strike vector.

434 Figure 6. The distance  $\Delta r$  from the central point on the lower datum to the closest point on the strike line  
435 on the upper datum is along the dip vector. If the distance from the source to the central point on the  
436 lower datum is  $r$ , then the distance to the strike line is  $r + \Delta r$ . The angle of the ray plane from the vertical  
437 is  $\theta$ .

438 Figure 7. The distance from the source location (\*) to the central point on the lower datum is  $r$ . The  
439 depth to the source  $d$  from the lower datum is  $r \cos \theta$ .

440 Figure 8. When the upward continued datum is two grid cells above the measurement datum, ray planes  
441 with angles less than 27 degrees (inside the dotted circle) can be determined reliably. Greater angles can  
442 be determined when the strike directions are close to 45 and 135 degrees.

443 Figure 9. The magnetic total field for a synthetic model containing a dyke buried at 5 km with a  
444 magnetization of 5 A/m (left feature); a vertical sided prism with a magnetization of 0.4 A/m and buried  
445 at a depth of 3 km (top right); and a larger vertical prism with a magnetization of 0.6 A/m and a depth to  
446 top of 7 km (bottom right). The magnetization is assumed induced by a vertical field.

447 Figure 10. The  $m$  values (where  $m = (dT/dx) / (dT/dz)$ ) for the synthetic data in Figure 9.

448 Figure 11. The strike angle estimated from the trend defined by the  $m$  values on the upper datum. Zero  
449 degrees corresponds to a north-south strike, 90 degrees is an east west strike and 180 degrees is also

450 north-south. Note the noise artifacts on the edges of the grid where the fields are small and the gradients  
451 weak.

452 Figure 12. The standard deviation of the strike estimates in Figure 11. Blue values imply a good estimate  
453 of the strike, warmer colours are poorer estimates.

454 Figure 13. The estimate of the structural index  $n$ .

455 Figure 14. The depth to the structure. The width of the coloured zone is also an indication of the depth.

456 Figure 15. Magnetic map showing the Saskatoon area. North is to the top. The area is 143 km wide and  
457 117 km high. Three asterisks are used to indicate narrow magnetic features.

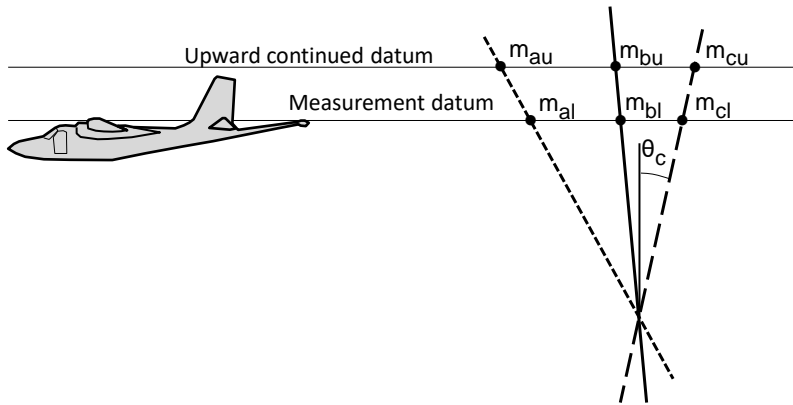
458 Figure 16. The structural index map of the Saskatoon area.

459 Figure 17. The depth map of the Saskatoon area.

460

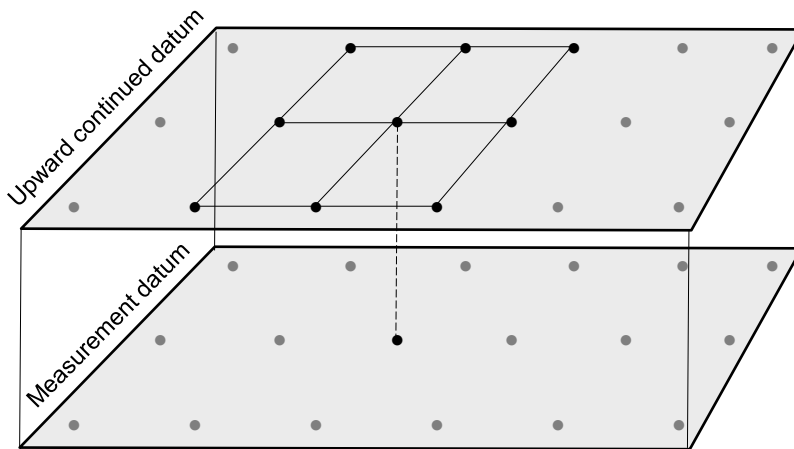
461

462  
463 **Figures**



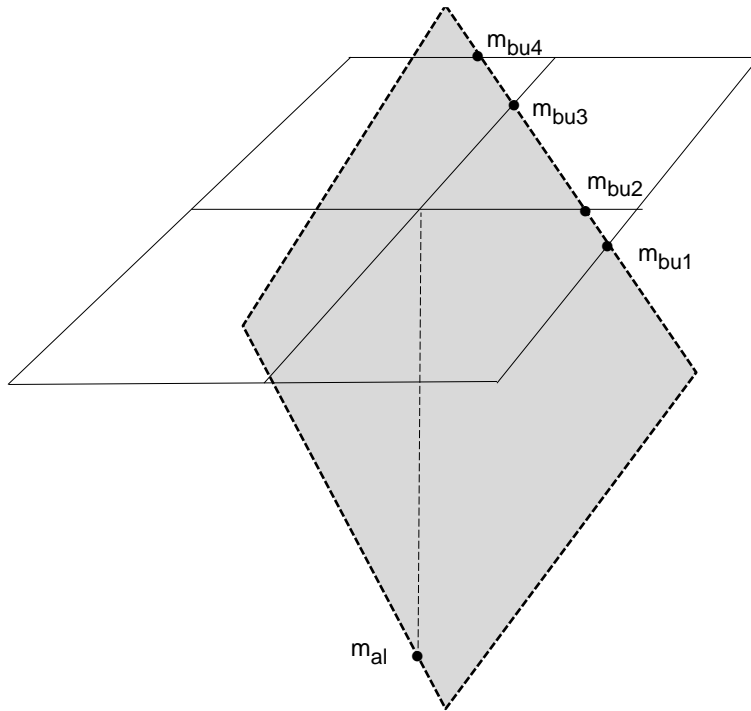
464

465 Figure 1. The basic principle of the SLUTH method. The field is measured on a measurement datum and  
466 upward continued to a higher datum. The horizontal and vertical spatial derivatives are calculated on  
467 both datums and the ratio used to calculate the  $m$  values. Rays are drawn along lines joining similar  $m$   
468 values on the two datums and these rays converge at the source location. The angle of the ray from the  
469 vertical is given by the angle  $\theta$ .



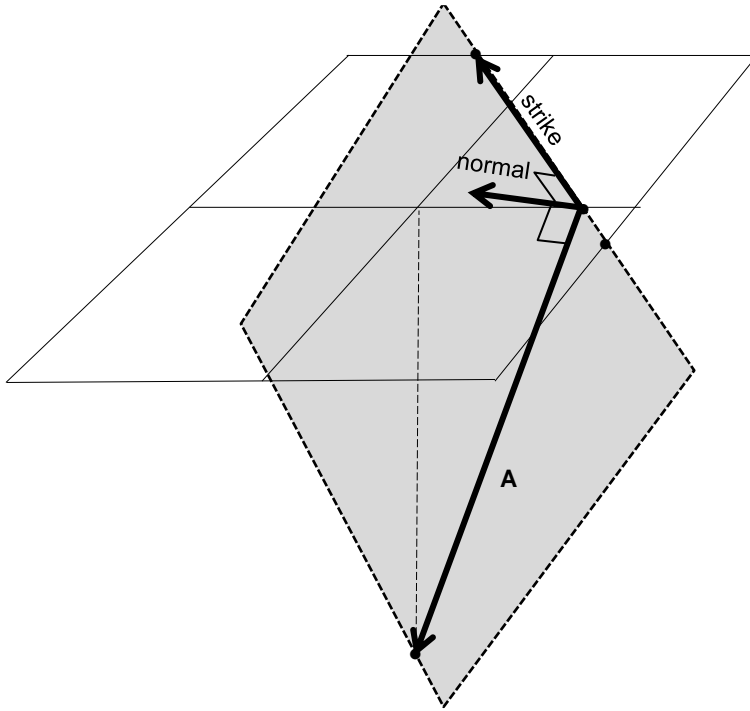
470

471 Figure 2. Oblique 3D view of the upper and lower datums. The dotted line joins a grid point on the  
472 upper datum directly above a point on the lower datum. There are nine points in a window on the upper  
473 datum (including the central point).



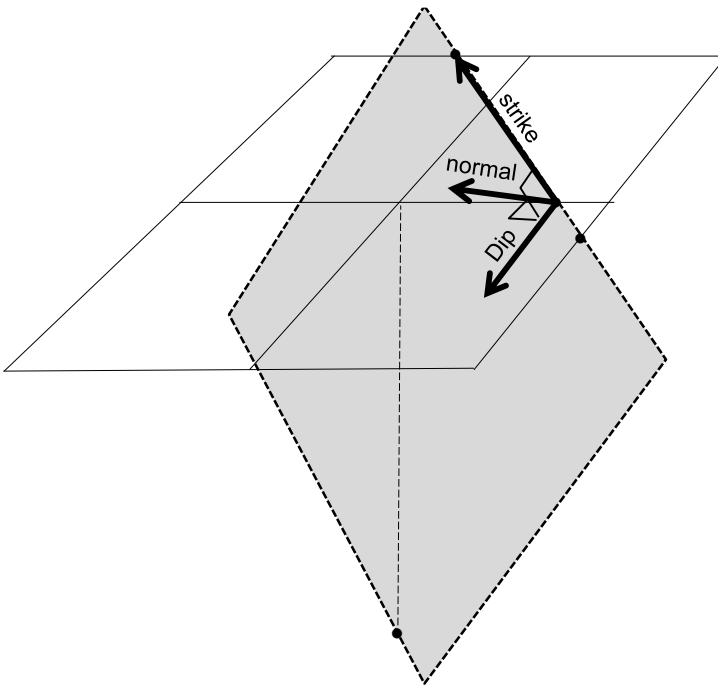
474

475 Figure 3. The  $m$  value at the central point on the lower datum is  $m_{al}$ . Similar values are sought on the  
 476 lines joining the 9 points on the upper datum. In this case, there are four points obtained, forming a  
 477 straight horizontal line. This line is the strike direction of the ray plane shown in grey, which is the  
 478 extension to 3D of the rays drawn on Figure 1. The source location is at greater depth on the ray plane,  
 479 where this ray plane intersects with another ray plane.



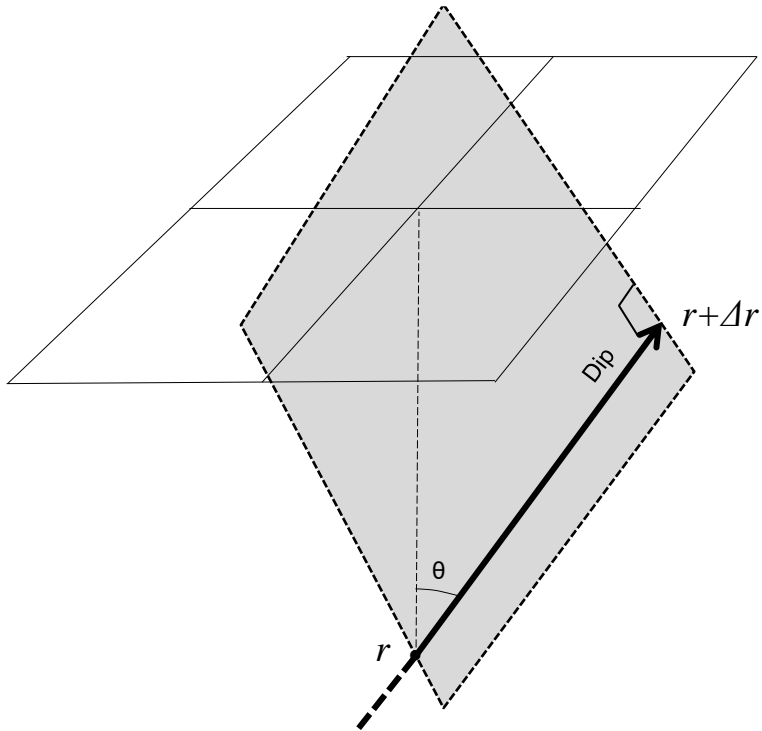
480

481 Figure 4. The normal to the ray plane can be obtained as the vector normal to any two non-parallel  
 482 vectors in the ray plane. In this case, the non-parallel vectors are the strike vector and the vector **A** from a  
 483 point on the strike line to the central point on the lower datum.



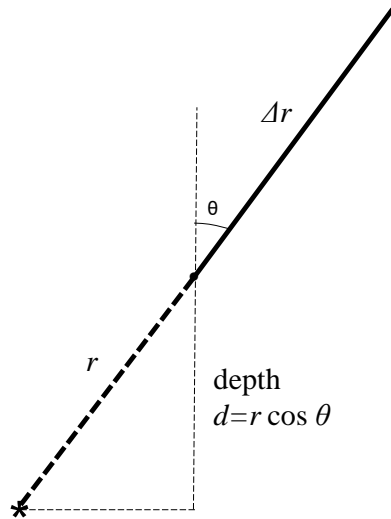
484

485 Figure 5. The dip vector is perpendicular to the normal vector and the strike vector.



486

487 Figure 6. The distance  $\Delta r$  from the central point on the lower datum to the closest point on the strike line  
488 on the upper datum is along the dip vector. If the distance from the source to the central point on the  
489 lower datum is  $r$ , then the distance to the strike line is  $r + \Delta r$ . The angle of the ray plane from the vertical  
490 is  $\theta$ .



491

492 Figure 7. The distance from the source location (\*) to the central point on the lower datum is  $r$ . The  
 493 depth to the source  $d$  from the lower datum is  $r \cos \theta$ .

494

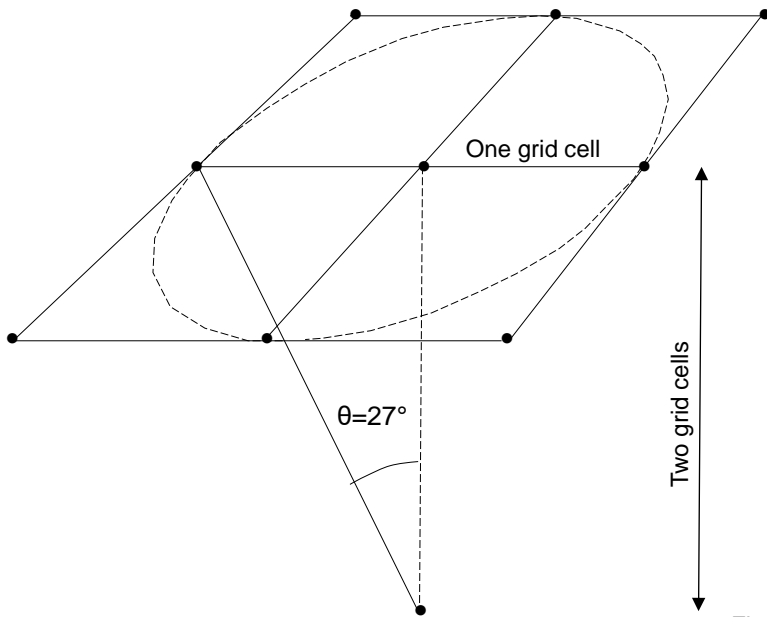
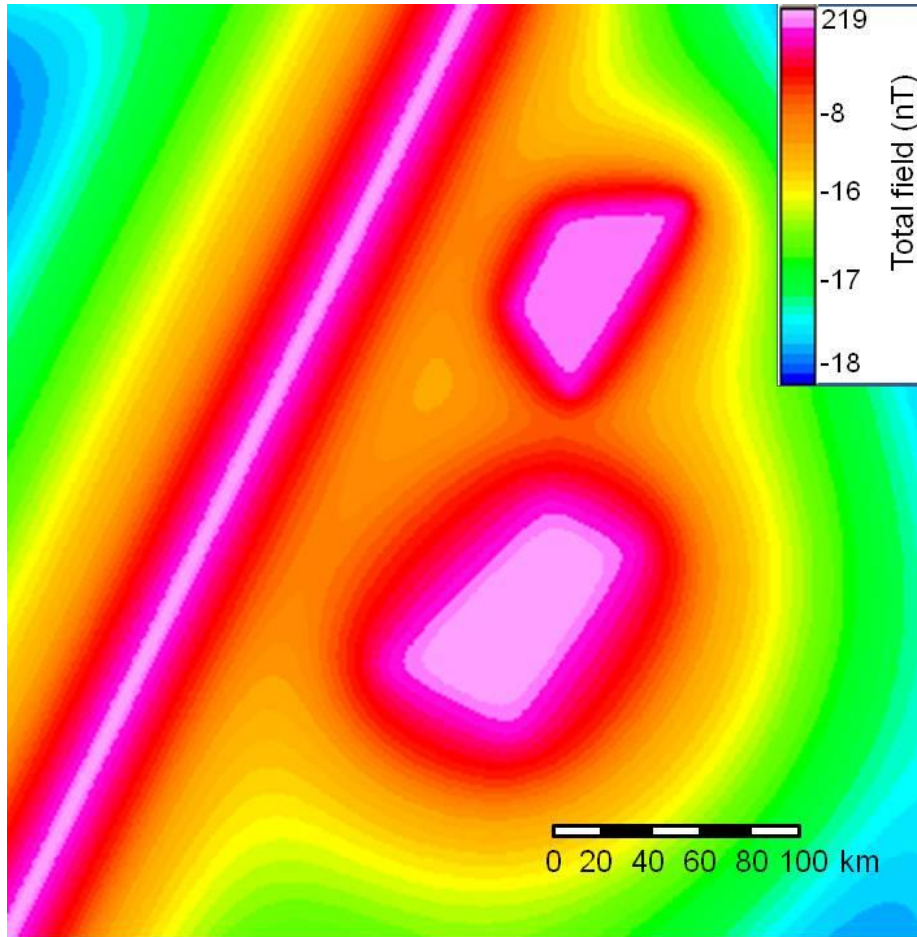


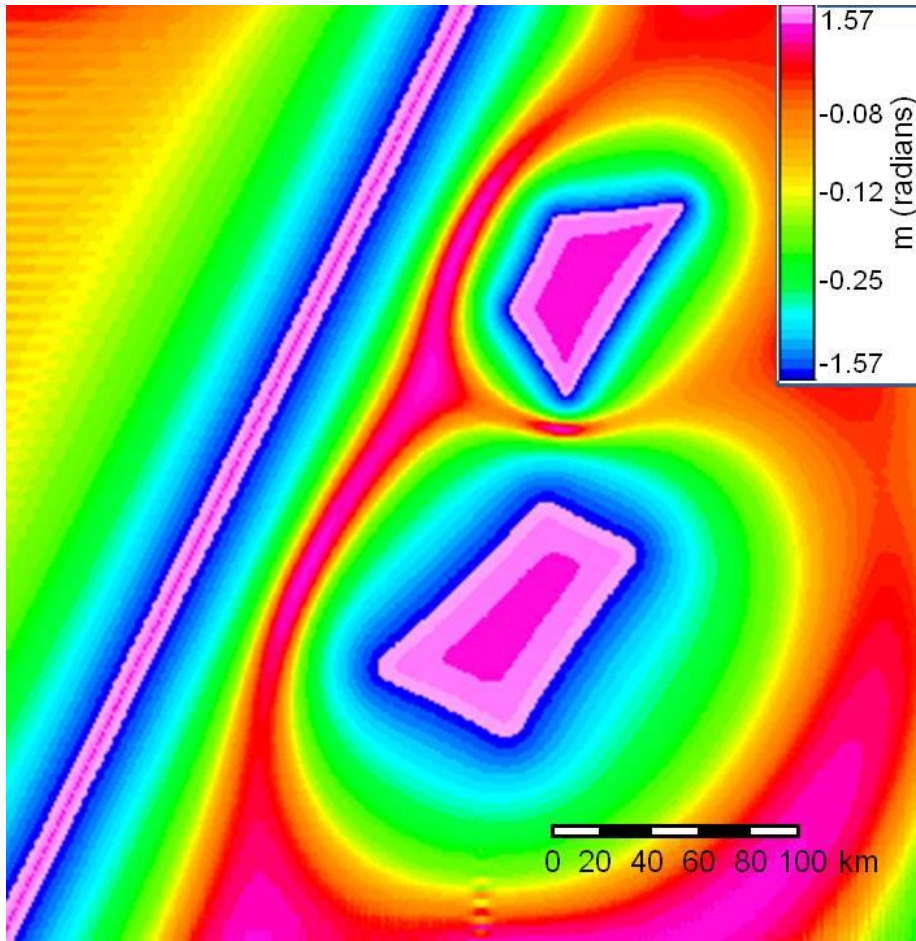
Figure 8

495

496 Figure 8. When the upward continued datum is two grid cells above the measurement datum, ray planes  
497 with angles less than 27 degrees (inside the dotted circle) can be determined reliably. Greater angles can  
498 be determined when the strike directions are close to 45 and 135 degrees.



499  
500 Figure 9. The magnetic total field for a synthetic model containing a dyke buried at 5 km with a  
501 magnetization of 5 A/m (left feature); a vertical sided prism with a magnetization of 0.4 A/m and buried  
502 at a depth of 3 km (top right); and a larger vertical prism with a magnetization of 0.6 A/m and a depth to  
503 top of 7 km (bottom right). The magnetization is assumed induced by a vertical field.



504

505 Figure 10. The  $m$  values (where  $m = (dT/dx) / (dT/dz)$ ) for the synthetic data in Figure 9.

506

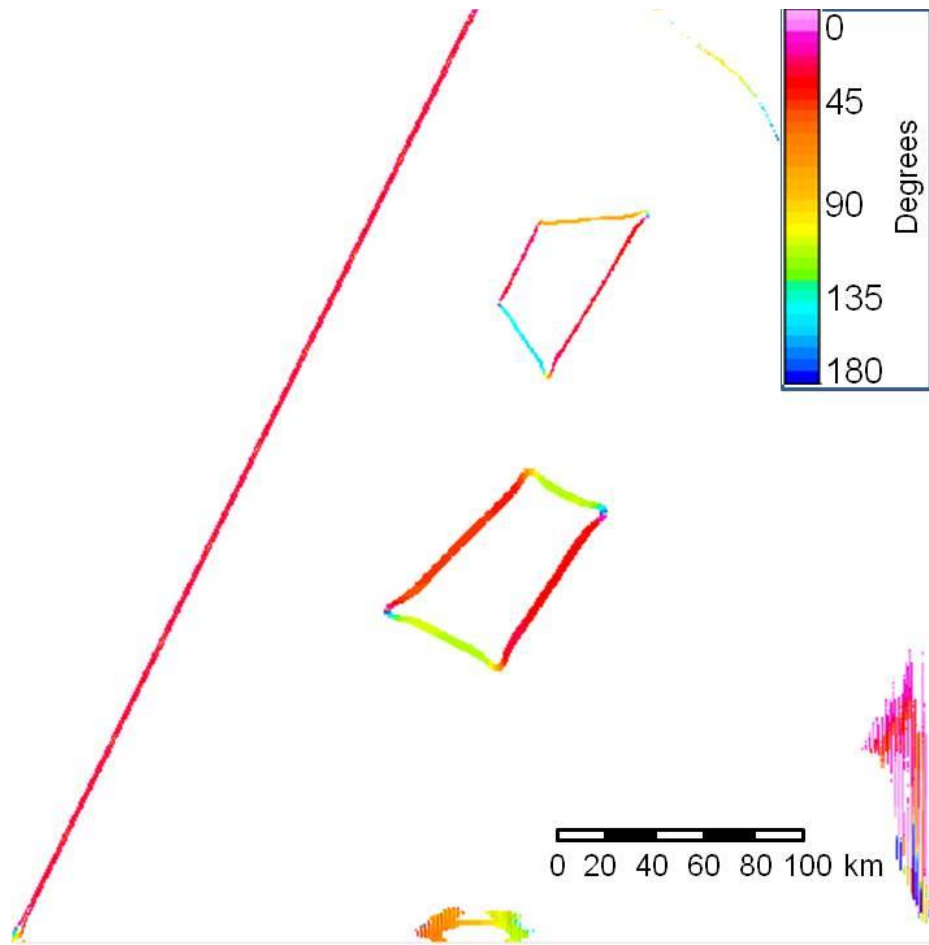


Figure 11

507  
 508 Figure 11. The strike angle estimated from the trend defined by the  $m$  values on the upper datum. Zero  
 509 degrees corresponds to a north-south strike, 90 degrees is an east west strike and 180 degrees is also  
 510 north-south. Note the noise artifacts on the edges of the grid where the fields are small and the gradients  
 511 weak.

512

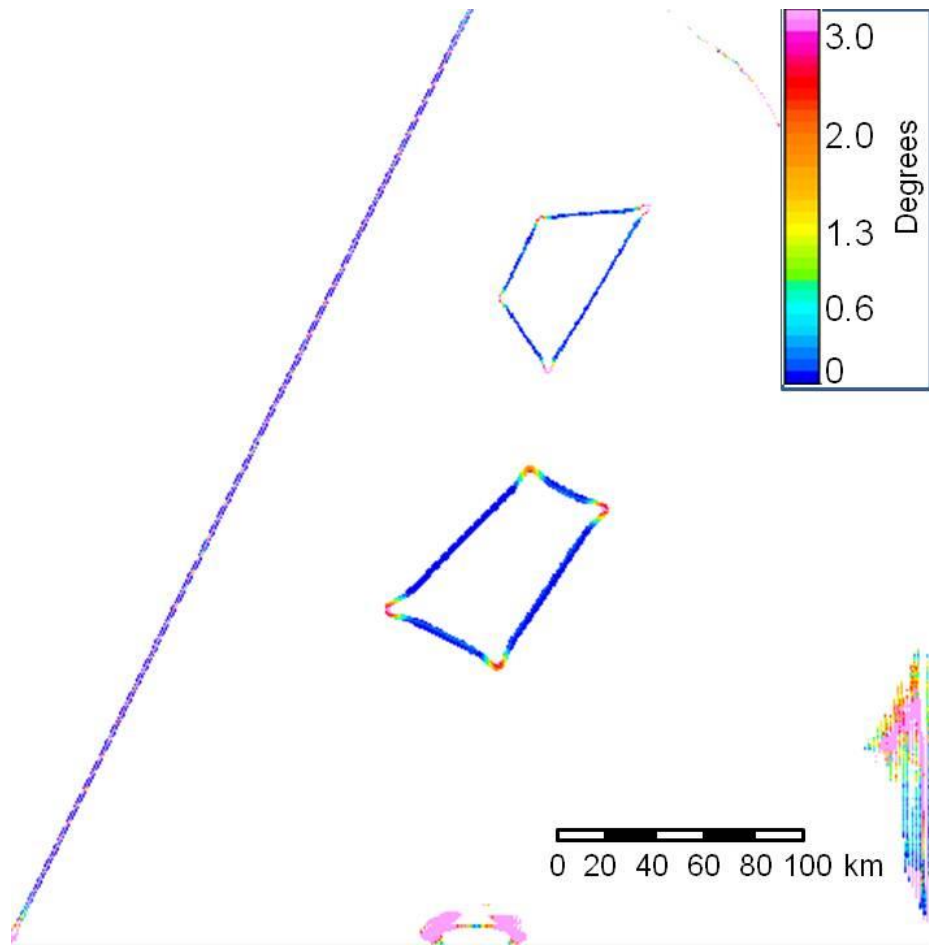


Figure 12

513  
 514 Figure 12. The standard deviation of the strike estimates in Figure 11. Blue values imply a good estimate  
 515 of the strike, warmer colours are poorer estimates.

516

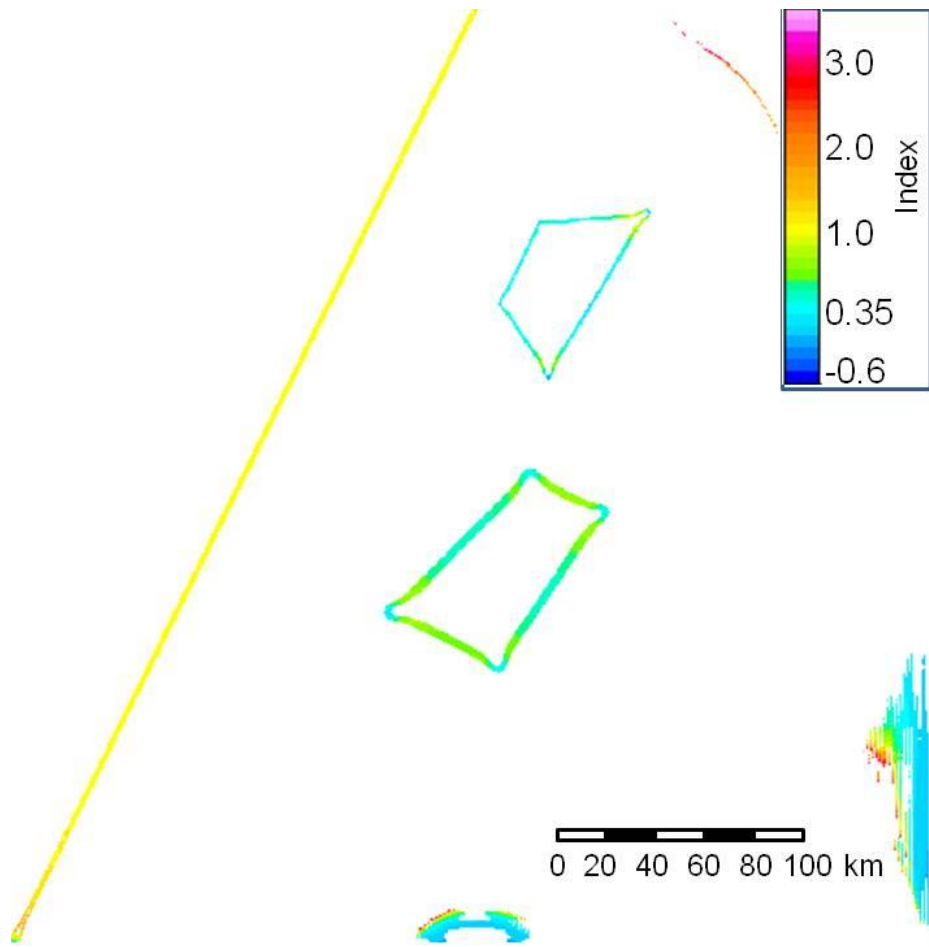


Figure 13

517  
518 Figure 13. The estimate of the structural index  $n$ .

519

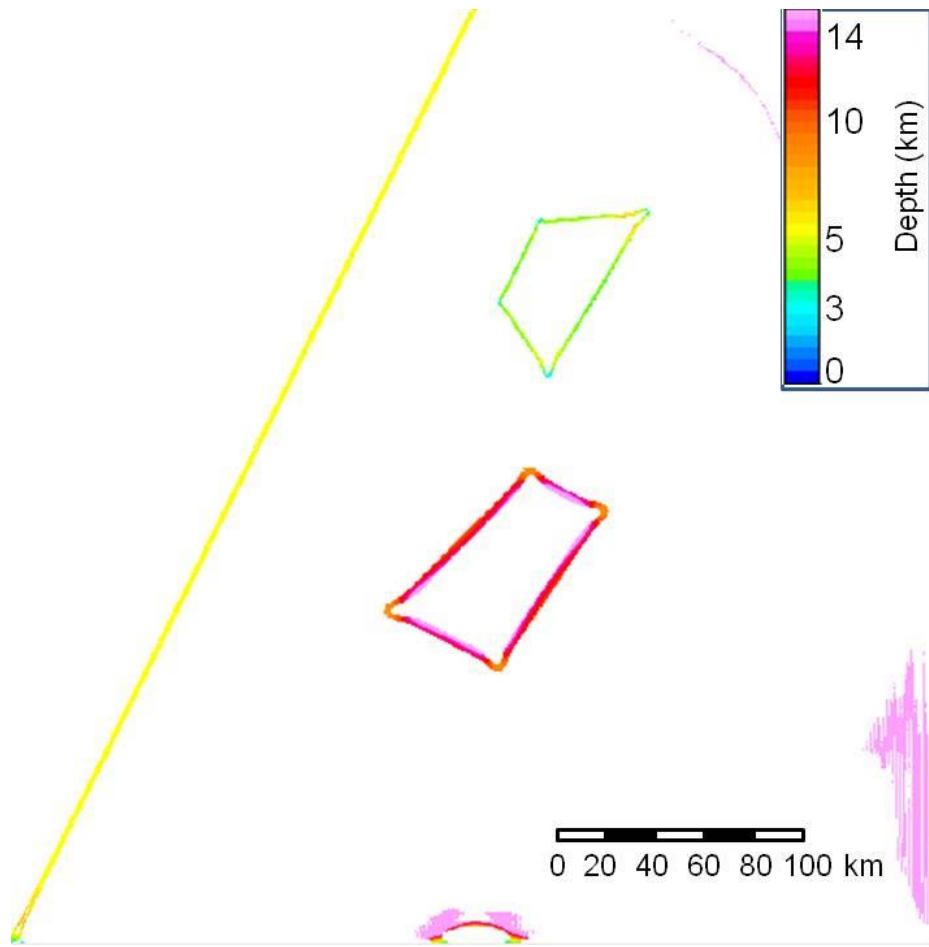


Figure 14

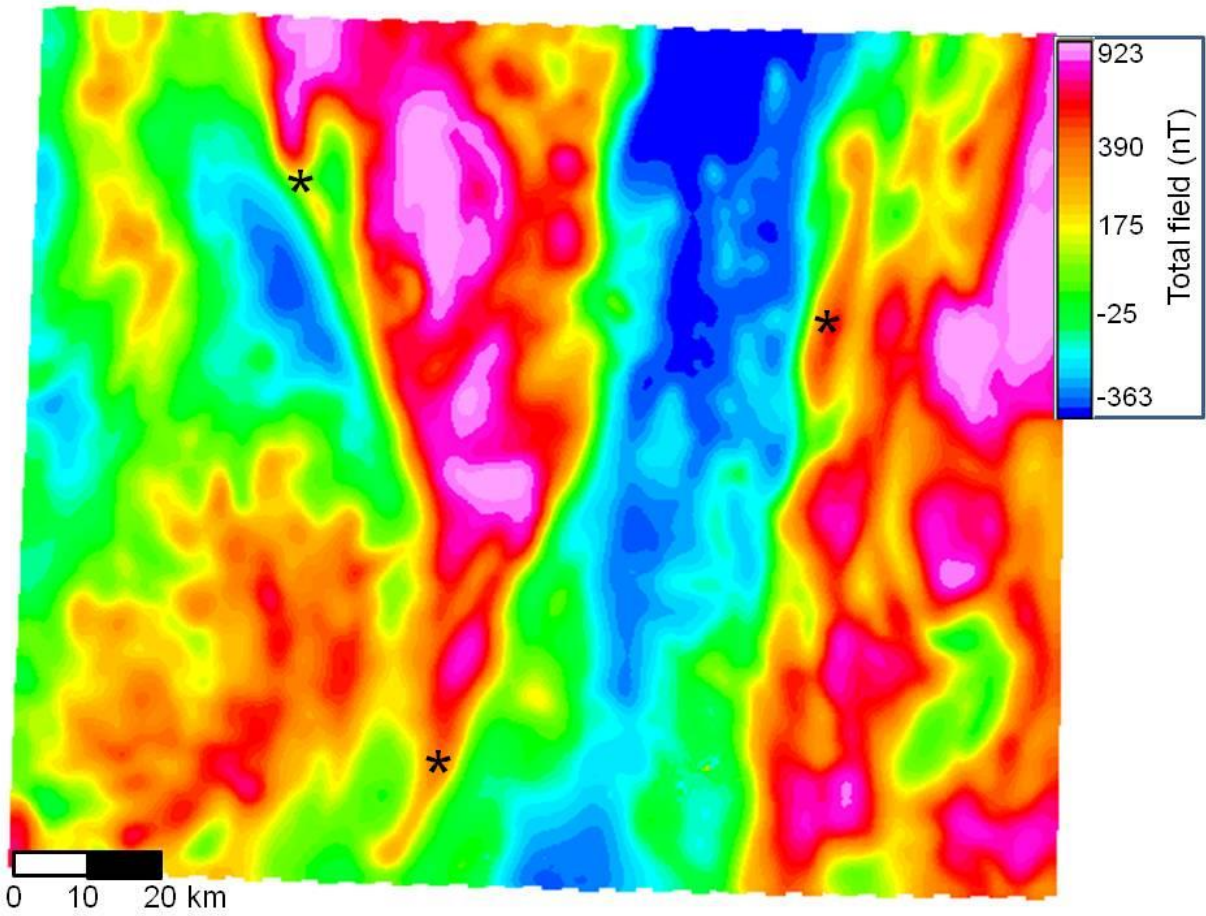
520

521

Figure 14. The depth to the structure. The width of the coloured zone is also an indication of the depth.

522

523



524

525 Figure 15. Magnetic map showing the Saskatoon area. North is to the top. The area is 143 km wide and  
526 117 km high. Three asterisks are used to indicate narrow magnetic features.

527

528

529

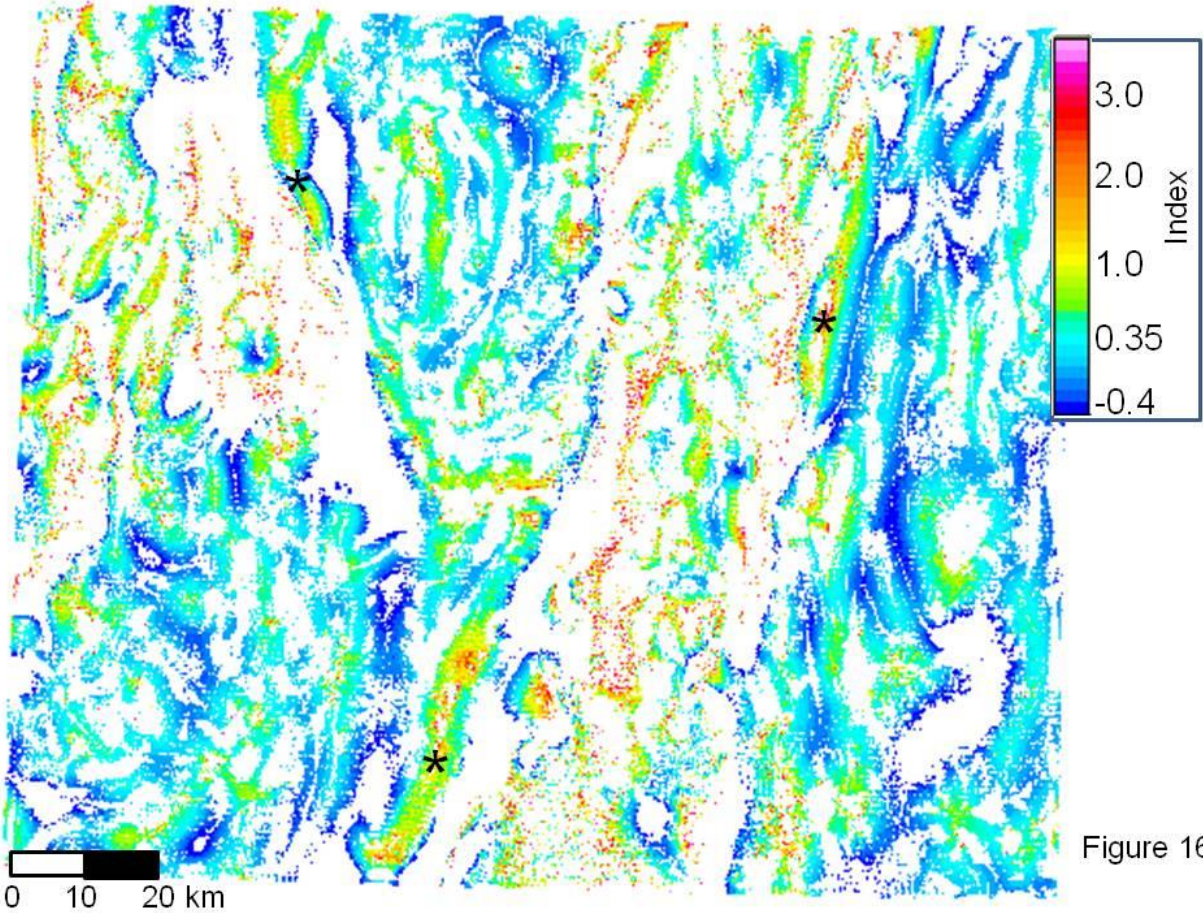


Figure 16

530

531 Figure 16. The structural index map of the Saskatoon area.

532

533

534

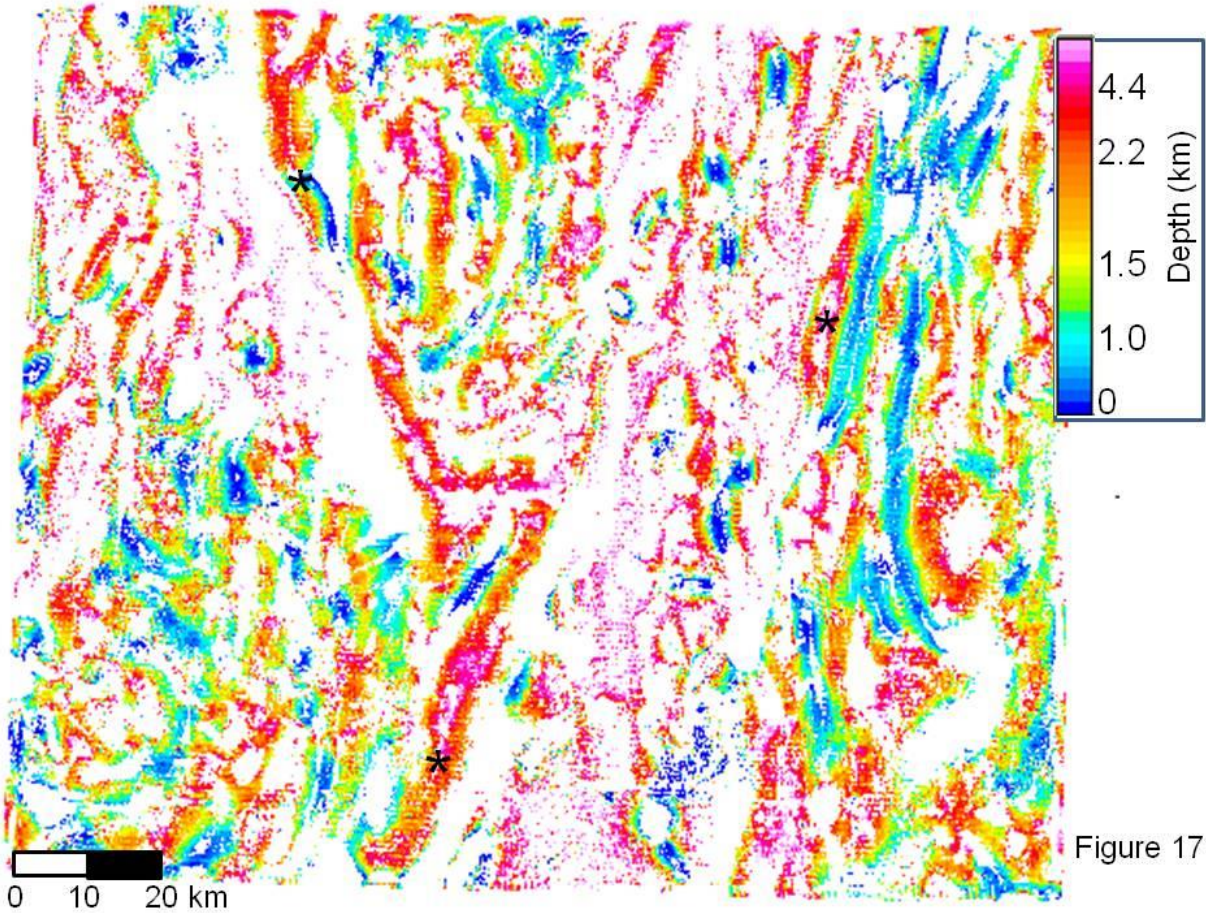


Figure 17

535  
536

Figure 17. The depth map of the Saskatoon area.